Detecting Anomalies Reliably in Long-term Surveillance Systems

Jinsong Liu[a], Ivan Nikolov[b], Mark P. Philipsen[c] and Thomas B. Moeslund[d]
Visual Analysis and Perception Laboratory, CREATE, Aalborg University, 9000 Aalborg, Denmark

Keywords: Surveillance, Anomaly Detection, Autoencoder, Long-term, Weighted Reconstruction Error, Background Estimation.

Abstract: In surveillance systems, detecting anomalous events like emergencies or potentially dangerous incidents by manual labor is an expensive task. To improve this, anomaly detection automatically by computer vision relying on the reconstruction error of an autoencoder (AE) is extensively studied. However, these detection methods are often studied in benchmark datasets with relatively short time duration — a few minutes or hours. This is different from long-term applications where time-induced environmental changes impose an additional influence on the reconstruction error. To reduce this effect, we propose a weighted reconstruction error for anomaly detection in long-term conditions, which separates the foreground from the background and gives them different weights in calculating the error, so that extra attention is paid on human-related regions. Compared with the conventional reconstruction error where each pixel contributes the same, the proposed method increases the anomaly detection rate by more than twice with three kinds of AEs (a variational AE, a memory-guided AE, and a classical AE) running on long-term (three months) thermal datasets, proving the effectiveness of the method.

1 INTRODUCTION

For a safer daily life, round-the-clock surveillance systems have been installed in some private and public places. Generally they are manually operated, which is expensive. Therefore, an automatic tool to help find emergencies or potentially dangerous incidents that require extra attention is in dire needed.

From the perspective of computer vision, such a tool can be realized using either supervised or unsupervised learning. Supervised learning needs a large amount of annotated data illustrating what the emergencies or potentially dangerous incidents look like. This is too expensive as collecting enough data of rarely-occurring incidents is time consuming and even unfeasible. On the contrary, unsupervised learning greatly lowers the cost, making it more preferred in this task.

This unsupervised solution is often realized by anomaly detection via an autoencoder (AE), which treats these rarely-happening emergencies and potentially dangerous incidents as anomalies but frequently-occurring incidents as normal. In general, an anomaly is deviating from a normal in many aspects. An AE trained with only normal data can reconstruct similar normal patterns with minimal errors, but struggles with abnormal patterns. Hence the difference between the input and the reconstructed out-

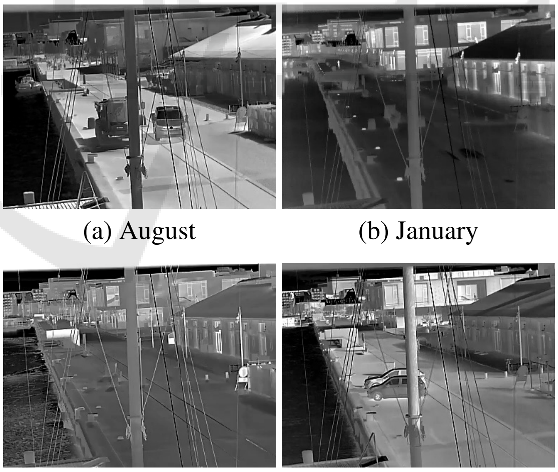

(a) August (b) January (c) February (d) April

Figure 1: Example images from different months. All show normal activity but with significant differences due to the seasons.

[a] https://orcid.org/0000-0002-5231-6950
[b] https://orcid.org/0000-0002-4952-8848
[c] https://orcid.org/0000-0002-9212-2544
[d] https://orcid.org/0000-0001-7584-5209

Liu, J., Nikolov, I., Philipsen, M. and Moeslund, T.
Detecting Anomalies Reliably in Long-term Surveillance Systems.
DOI: 10.5220/0010907000003124
In *Proceedings of the 17th International Joint Conference on Computer Vision, Imaging and Computer Graphics Theory and Applications (VISIGRAPP 2022) - Volume 4: VISAPP*, pages 999-1009
ISBN: 978-989-758-555-5; ISSN: 2184-4321

put, usually in the form of mean square error (MSE), has the ability to measure the input's deviation from the normal data. Input with the MSE larger than a predefined threshold is detected as an anomaly.

This detection strategy works with an assumption that the concept of what is normal is constant. Benchmark datasets on which existing anomaly detection solutions are evaluated satisfy this assumption, because they are relatively short in time duration. However, in real life a surveillance system will be running for months and hence the normal pattern will inevitably drift. This can be illustrated in Figure 1 where all these four harbor front scenes are normal in terms of human activities, but the obvious changes across time in contrast, illumination, water ripples, and other environmental aspects make them different from what has been defined as normal in the training phase. This time-induced drift has a large influence on the reconstruction error and thus the anomaly detection is not reliable any more. This phenomenon raises an open research question — how to detect anomalies reliably in long-term surveillance systems.

To this end, we propose a weighted reconstruction error method that uses different weights for foreground pixels and background pixels in calculating the error, for which five background estimation (foreground extraction) methods are implemented and evaluated. In this way, the influence of the time-induced drift on the reconstruction error is reduced and hence anomaly detection is more reliable.

By applying the proposed method to long-term datasets spanning three months (August 2020, January 2021, April 2021) collected from a real-world harbor front surveillance system, the experimental results show that the weighted reconstruction error increases the anomaly detection rate by at least twice than that with the conventional reconstruction error, for all the three kinds of AEs (a variational AE, a memory-guided AE, and a classical AE), proving the effectiveness of the method.

The datasets and code are published on GitHub — https://github.com/JinsongCV/Weighted-MSE, making the integration of the weighted reconstruction error and the comparison between before and after results much easier.

2 RELATED WORK

Existing work on anomaly detection (Hasan et al., 2016; Chong and Tay, 2017; Fu et al., 2018; Yue et al., 2019; Nguyen and Meunier, 2019; Song et al., 2019; Gong et al., 2019; Deepak et al., 2020; Tsai and Jen, 2021; Liu et al., 2021b) is usually AE-based.

Table 1: Time duration (hours) of benchmark datasets for anomaly detection.

Avenue	ShanghaiTec	UCSD	UMN	Subway
0.5	3.6	3.1	0.07	2.3

Though some attempts are made to improve the anomaly detection performance, for example incorporating temporal information (Fu et al., 2018; Yue et al., 2019; Nguyen and Meunier, 2019), introducing a generative adversarial network (GAN) to differentiate reconstructions from inputs (Song et al., 2019), using both the memorized features of the training set and the input's features to do reconstruction (Gong et al., 2019; Park et al., 2020), and so on, these methods are only studies on benchmark datasets — Avenue (Lu et al., 2013), ShanghaiTech (Luo et al., 2017), UCSD (Mahadevan et al., 2010), UMN (Mehran et al., 2009), and Subway (Adam et al., 2008)), which have an imperfection in common — a short duration of a few minutes or hours (shown in Table 1) (Pranav et al., 2020; Nikolov et al., 2021). Therefore, generalizing the existing work evaluated on such datasets to a long-term application in real life can be problematic, considering the extra time-induced changes. For example, the illumination and contrast vary from the shifts in day and night, weather, seasons, etc. This environmental drift imposes an additional variation on the reconstruction error and thus makes it not solely correlated to human activities that are responsible for most anomalies.

This challenge inspires us to focus more on foreground regions where anomalies are assumed in when calculating the reconstruction error, to eliminate the influence of the time-induced environmental drift, which is exactly the proposed weighted reconstruction error does.

A similar solution to ours is the object-centric AE (Ionescu et al., 2019; Georgescu et al., 2020) that takes the pre-detected object region instead of the full image as the input. Despite the similarity, there are four distinctions. (i) The goals are different. Their work expects to generalize an AE trained on one scene to another scene without further finetuning, while our method targets to reduce the effect of the environmental drift in long-term surveillance systems. (ii) Our method still reconstructs the full image instead of only object regions, because the location of an object relative to the background is important, for example, a drowning accident only happens in the water area. (iii) Our method is much more flexible like a post-processing module and thus easily incorporated to any framework. (iv) Our method treating foreground and background regions separately also provides an ability to investigate environmental anomalies like a sudden contrast change due to an extreme weather event.

3 METHODS

This paper proposes a weighted reconstruction error for anomaly detection illustrated by the diagram in Figure 2.

In it, the red flow indicates the conventional anomaly detection scheme where the reconstruction error (in the form of MSE) is directly calculated from the input and the reconstructed output with each pixel contributes the same. This calculation also considers the time-induced environmental drift as part of the reconstruction error, and thus for input spanning a long time period the MSE curve will fluctuate greatly. This is very dangerous as a real anomaly will be ignored, if its MSE value is lower than other fluctuated MSE values of normal inputs. Such a phenomenon is shown in the upper MSE curve where normal inputs with drift have larger MSE values than the threshold (the red dashed line), not only introducing false positives but also missing the real anomaly.

In contrast, the green flow in the diagram indicates the proposed weighted reconstruction error-based anomaly detection scheme. Additional background estimators or object-centric foreground extractors can segment an input into foreground region and background region. This information together with the input and the reconstruction are used to calculate the reconstruction error where the foreground pixels and background pixels are assigned different weights, so that the error focuses more on the region where anomalies usually happen and thus the effect of the environmental drift is reduced. In this way, the weighted MSE curve will be much more smoother for normal inputs but generates a peak if an anomaly comes in, like the lower W-MSE curve shows. Another thing to be mentioned is that both the red flow scheme and the proposed green flow scheme are indicating the inference phase — anomaly detection.

3.1 Autoencoder

Following what is customary, we use an AE to detect anomalies by finding frames with the largest reconstruction errors. Three AEs are applied. The first is a variational AE — VQVAE2 (Razavi et al., 2019) whose encoder compresses the input into multi-scale quantized latent maps for the decoder to process. The second is a memory-guided AE — MNAD (Park et al., 2020) that uses a concatenated latent space (of the naive latent space from the encoder output and the typical features stored in a memory module constructed from training) to reconstruct the input. An anomaly is measured by not only the reconstruction error but also the distance between the encoder output and the nearest memorized features. The third is a classical AE (CAE) designed by us, which is without any advanced processing of the latent space. This CAE uses eleven convolution layers and five pooling layers to downsize the input ($384 \times 288 \times 1$) into a compressed feature tensor ($10 \times 7 \times 64$), and another six transposed convolution layers and five convolution layers to transform the latent feature space into the reconstructed output. Detailed implementations are shared on GitHub.

3.2 Background Estimation

As mentioned before, the method is characteristic of foreground regions and background regions contributing differently to the weighted reconstruction error. Therefore, separating the background from the foreground is the key. To achieve this we test out two pipelines, one using classical statistical methods to estimate the background, the other one using the result of a human detector as the foreground and everything else as the background.

In section 4, we will test all the methods of the two pipelines and determine which is the best method or the best combination of a few methods to separate the foreground from the background, so that the drift can be removed effectively for improving the anomaly detection rate.

3.2.1 Statistical Background Estimation

This pipeline is composed of classical statistical approaches instead of deep learning segmentation methods (Babaee et al., 2018; Akilan et al., 2019) to minimize the complexity. Also this avoids the high price of supervised segmentation concerning pixel-level annotations. In our harbor front scenario, the objects in the foreground vary significantly — humans from a single one to groups, vehicles, bicycles, and others. These variations cause extra difficulties and manpower in pixel-level annotations if a deep model is chosen. The four classical background estimators are as follows:

- Mixture of Gaussians (MOG2) (Zivkovic, 2004) — using Gaussian mixture probability density to continuously model the background.
- Mixture of Gaussians using K-nearest neighbours (KNN) (Zivkovic and Van Der Heijden, 2006) — an extension of the MOG2 method by implement-

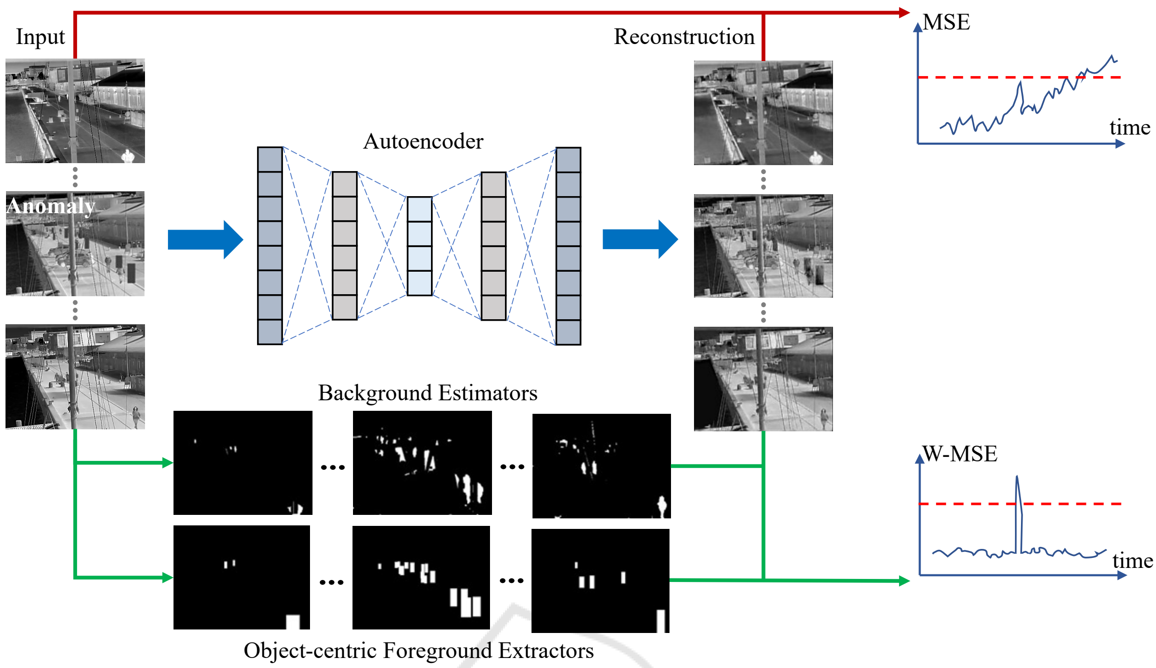

Figure 2: Diagram of the proposed method.

ing a K-nearest neighbours algorithm on top for a more robust kernel density estimation.

- Image difference with arithmetic mean (ID_a) — the difference between the current image and the previous one is processed by adaptive thresholding to get the background mask. ID_a uses an arithmetic mean weight — each pixel in the neighborhood contributes equally to compute the local threshold.
- Image difference with Gaussian mean (ID_g) — the same principle with ID_a, but with a different adaptive thresholding strategy. ID_g uses a Gaussian mean weight — pixels in the neighborhood farther away from the center contribute less to the local threshold computing.

To do background estimation, all the four methods need the neighbouring images of the current frame. For the MOG2 and KNN methods, the number of neighbouring images is heuristically set to 20, as it has been shown that more frames are better at modeling the background. For the ID_a and ID_g methods, only one previous image is used.

Once a mask is acquired from any of the four methods, it goes through a post-processing procedure — a morphological closing with a structuring element of size 7×7 followed by an opening with an element of size 3×3. This step serves to remove small noise particles. Finally, the moving elements in the background like the water, ropes, and masts are removed from the mask by prior knowledge of their locations. The resulting mask will have foreground pixels with large grayscale values approaching 255 and background pixels with small values near 0. All of these procedures are implemented from the OpenCV library (Bradski, 2000).

3.2.2 Object-centric Foreground Extraction

Besides the above four classical approaches, we test another method — object-centric foreground extraction, provided that there is a well-trained human detector at hand and human activities are the targets. The detector we use is YOLOv5 (Ultralytics, 2020; Liu et al., 2021a), with which each person is represented by a rectangle in the mask. The pixels in the rectangle has a same grayscale value — the person's detection confidence multiplied by 255, while pixels in other regions are with the value 0.

As a whole, these five versions of masks explicitly locate foreground areas with very large grayscale values, so for a clear reference the subsequent contents will call such a mask foreground map. Figure 3 shows one input image and the results from the five methods.

3.3 Weighted Reconstruction Error

First to be noted is that this paper goes with the convention and thus opts for the MSE to measure the difference between the input and the reconstructed output, so the following contents will directly use MSE to represent the difference without further explanation.

(a) Input (b) MOG2 (c) KNN (d) ID_a (e) ID_g (f) YOLOv5

Figure 3: An input thermal image and the outputs from the five implemented background estimation (foreground extraction) methods.

As long as there is a foreground map M locating foreground pixels P_{fg}, any weighted MSE is possible by giving P_{fg} and background pixels P_{bg} arbitrarily-defined weights for a specific task.

For an input I with size $H \times W$ and its corresponding reconstruction R, a general weighted MSE_w is:

$$MSE_w = \frac{\sum_{i=1}^{H}\sum_{j=1}^{W}(I_{ij} \cdot \bar{M}_{ij} - R_{ij} \cdot \bar{M}_{ij})^2}{H \times W} \quad (1)$$

where $\bar{M}_{ij}$ is the value of the weight map $\bar{M}$ at pixel (i, j). $\bar{M}$ is calculated using Equation 2.

$$\bar{M} = \frac{w_{fg} \times M + w_{bg} \times (255 - M)}{255} \quad (2)$$

where w_{fg} and w_{bg} are normalized weights for P_{fg} and P_{bg}, respectively; as an 8-bit image, $255 - M$ is the "inverse" operation of M, explicitly locating P_{bg}; therefore $\bar{M}$ is the final weight map normalized to 0-1 for calculating weighted MSE in Equation 1.

Setting w_{fg} as 1 and w_{bg} as 0 is the special case of the MSE only considering P_{fg}. Likewise, setting w_{fg} as 0 and w_{bg} as 1 is the MSE only looking at P_{bg}.

A more general case is a weighted MSE_w combining foreground maps (e.g., M_1, M_2) from several background estimators (foreground extractors).

$$MSE_w = \frac{\sum_{i=1}^{H}\sum_{j=1}^{W}(I_{ij} \cdot \bar{M}_{ij} - R_{ij} \cdot \bar{M}_{ij})^2}{H \times W} \quad (3)$$

$$\bar{M} = w_1 \times \bar{M}_1 + w_2 \times \bar{M}_2 \quad (4)$$

$$\bar{M}_1 = \frac{w_{fg_1} \times M_1 + w_{bg_1} \times (255 - M_1)}{255} \quad (5)$$

$$\bar{M}_2 = \frac{w_{fg_2} \times M_2 + w_{bg_2} \times (255 - M_2)}{255} \quad (6)$$

where, $\bar{M}_1$ is the weight map from M_1 with w_{fg_1} and w_{bg_1} as normalized weights for P_{fg} and P_{bg} in M_1; $\bar{M}_2$ is the weight map from M_2 with w_{fg_2} and w_{bg_2} as normalized weights for P_{fg} and P_{bg} in M_2; $\bar{M}$ is the final weight map combining $\bar{M}_1$ with weight w_1 and $\bar{M}_2$ with weight w_2; the resulting MSE_w is the weighted MSE considering foreground maps from two methods.

4 EXPERIMENTS

4.1 Dataset Information

Two datasets collected from a long-term harbor front surveillance system are used to investigate the proposed weighted MSE on anomaly detection.

One dataset called 300Ver has 300 images with every 100 sampled from August 2020, January 2021, and April 2021, making itself a dataset spanning 76 days. This dataset is a subset of a larger one covering 8-month and publicly available as part of the publication (Nikolov et al., 2021). The sampling protocol for 300Ver is also given in (Nikolov et al., 2021) which uses the temperature as a basis to construct datasets covering cold, warm, and in-between months.

The other dataset called 3515Ver is also a subset of the dataset from (Nikolov et al., 2021), and has 3515 images intensively sampled with a frame rate of 0.5fps from 15 pm to 18 pm from 14-16 August 2020, 14-16 January 2021, and 14-16 April 2021. This sampling protocol comes from three strategies. (i) Empirically 15 pm to 18 pm is the time period when there are most people present in view. (ii) Three days from each month not only guarantee the data diversity across time but also limit the amount of the dataset for better visualization in section 4.3.3. (iii) 0.5fps limits the amount of 3515Ver, at the same time keeping the information continuity between neighboring frames.

In 300Ver persons are annotated with bounding boxes. Therefore, six foreground maps from MOG2, KNN, ID_a, ID_g, YOLOv5, and ground truth (GT), are prepared for each image. The 3515Ver dataset has no such annotations, so only five kinds of foreground maps are calculated.

First the 300Ver dataset is used and the related experiments are in sections 4.3.1 and 4.3.2. The 3515Ver dataset is then used to verify what has been found on 300Ver and the related contents are in section 4.3.3. There are three reasons why we do experiments on both datasets. (i) 300Ver covers 76 days with less images while 3515Ver have more images but only covering 9 days; these two datasets compensate for each other, making the experiments consider both a long-term duration and a large amount of images. (ii) This separation of two datasets avoids the problem that if all the images are sampled intensively from the 76 days, the resultant 30000 images will make the visualization of drawing the MSE values of them into one curve (like the curve in the following contents) extremely difficult. (iii) Annotating a small dataset (300Ver) is much easier to provide a very accurate foreground extraction, based on which the findings of section 4.3.1 will be more convincing.

4.2 Implementation Details

Both VQVAE2 and MNAD are trained with 4000 images and validated with 1000 images. CAE is trained with 15000 images and validated with 5000 images due to its naive function compared with the other two. VQVAE2 is trained with a batch size of 32 and a learning rate of 0.0001. MNAD is trained with a batch size of 32, a learning rate of 0.0002, and a value of 0.1 for the weight of the feature separateness and compactness loss. CAE is trained with a batch size of 16 and a learning rate of 0.0003. The training phases stop at the 100th epoch, the 100th epoch, and the 200th epoch for VQVAE2, MNAD, and CAE, respectively, at which the networks are converged with the training losses not decreasing any more. All these training and validation sets are sampled from February 2021 to not only avoid the overlapping with the three-month datasets this paper uses but also enhance the effect of the time-induced drift that we want to address. A kind reminder is that the following experiments are done with all these three AEs but we usually only show related visualizations of VQVAE2 to avoid the repeat of similar results.

The YOLOv5 detector uses a pretrained model from (Liu et al., 2021a) and the training set has no overlapping with the images we use in this paper.

4.3 Weighted MSE

4.3.1 Weighted MSE Curves

To simplify the work and directly answer the question how the conventional MSE and weighted MSE behave for long-term datasets, according to Equation 1 and Equation 2, the MSE investigated will consider three situations: the foreground only, the background only, and the full image where each pixel contributes the same as the convention, which are represented as MSE_{fg}, MSE_{bg}, MSE_{cvt}, respectively. These representations will be used in all the following contents.

Therefore, for each AE with 300Ver as input, six kinds of foreground maps produce six MSE_{fg} curves and six MSE_{bg} curves describing the weighted MSE changes across time; likewise, one MSE_{cvt} curve can be drawn to describe the conventional MSE changes across time.

For a better comparison, Figure 4 shows the above mentioned 13 MSE curves, produced by the VQVAE2 model. This visualization (of showing multiple curves in one chart) is achieved with a critical pre-processing module before plotting: first the original MSE values are smoothed by a mean filter with its kernel size as 10; then the smoothed values are normalized between 0 and 1; after normalization the curves are overlapped with each other, so a further translation is done for each curve by adding an extra value. In this way, the ranges of curves of MOG2, KNN, ID_a, ID_g, YOLOv5, and GT are $[2.5, 3.5]$, $[2.0, 3.0]$, $[1.5, 2.5]$, $[1.0, 2.0]$, $[0.5, 1.5]$, $[0, 1]$, respectively; the range of the conventional MSE curve is $[3.0, 4.0]$.

From Figure 4 several observations are found. (i) The six MSE_{fg} curves in (a) have totally different trends with the trends of MSE_{bg} curves in (b), which is reasonable as the image regions they look at are not the same. (ii) The MSE_{cvt} curve in (b) has almost exactly same trend with that of the six MSE_{bg} curves in (b), but largely deviates from the trends of MSE_{fg} curves in (a), proving that on 300Ver the conventional MSE (where each pixel in the full image contributes the same) cannot represent what happens in the foreground region and thus have no ability to do anomaly detection reliably. (iii) Though the six MSE_{fg} curves in (a) are diverse, they share a similar trend to some extent especially between the MSE_{fg} curve of YOLOv5 and the MSE_{fg} curve of GT. This reflects that they have the ability to represent the foreground changes along with time but also have their own focuses shown by distinct peaks due to the methods' differences. The MSE_{fg} curve of YOLOv5 and the MSE_{fg} curve of GT are bounding box-based focusing only on persons, therefore a larger similarity is found between them. (iv) The trends of all the MSE_{bg} curves and the MSE_{cvt} curve in (b) are U-shape, revealing the influence of the drift across time on the MSE as mentioned before. However, the U-shape trend is not shown in foreground MSE curves in (a), indicating that the time-induced effect influences background regions higher than foreground regions. Hence researches on long-term datasets (applications) need separate analysis on them.

In addition to this, experiments done with MNAD and CAE also get similar results that all support the above findings. As a whole, this part confirms that in long-term datasets (applications) with time-induced drift, the conventional MSE (where each pixel contributes the same) is not suitable to describe the fore-

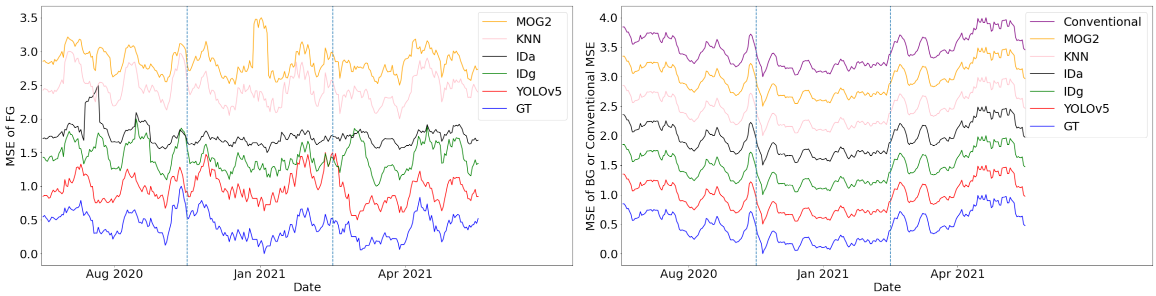

(a) MSE_{fg} (b) MSE_{bg} and MSE_{cvt}

Figure 4: MSE (after smoothing, normalization, and translation) curves across time from VQVAE2 on 300Ver. The vertical azure dashed lines are used to separate different months.

ground information, not to mention a further step — detecting anomalies.

4.3.2 Weighted MSE for Anomaly Detection

This section will test whether the proposed weighted MSE performs better in anomaly detection. Since there are no specified anomalies in the dataset, and detecting specific anomalies is not the focus of this work, we decide to use a strategy that maximizes the difference between an anomaly and a normal image, to better focus on the main research problem — how to do anomaly detection reliably in long-term datasets.

To realize this, we synthesize anomalies by overlapping "black-white-pixel" patterns (that the three AEs have never seen) on the person regions of some images. But it seems that such patterns overlapped on only person regions will give the YOLOv5-based foreground map a biased advantage. Hence, to evaluate the five kinds of foreground maps more fairly, four shapes (rectangle, square, circle, and ellipse) of the "black-white-pixel" pattern are considered for the reason that the detector-based map has no round-cornered foregrounds but the other four kinds of maps have. We admit this four-shape strategy cannot totally remove the bias on the YOLOv5-generated map, but if we put the "black-white-pixel" pattern on other foreground regions where there are no people, a greater bias will be given to other statistical background estimators because YOLOv5 only predicts human regions. Therefore, this four-shape strategy should be the best solution to treat these five kinds of foreground maps equally.

Accordingly, on the premise of having at least one person in each synthesized anomalous image, 21 rectangle-shaped anomalies (the 1st, 11st, 21st, ..., 281st images of 300ver), 21 square-shaped anomalies (the 3rd, 13rd, ..., 293rd images of 300ver), 20 circle-shaped anomalies (the 2nd, 12nd, ..., 282nd images of 300ver), and 16 ellipse-shaped anomalies (the 4th, 14th, ..., 284th images of 300ver) are synthesized. In each of them the annotated GT person regions are randomly chosen to be overlapped with "black-white-pixel" patterns. Examples of the synthesized anomalies are shown in Figure 5.

First, the rectangle-shaped anomalies are used to test the anomaly detection rate. Accordingly, in Figure 6, six MSE curves (five MSE_{fg} curves and one MSE_{cvt} curve) of VQVAE2 are drawn in color blue, and the anomalies are located with orange peaks. Each sub-figure caption has the same meaning with what has been used in section 4.3.1.

From Figure 6, the large percentage of overlapping between orange peaks and blue peaks in (a)-(e) proves the usefulness of the proposed weighted MSE in anomaly detection. This also happens in the experiments of VQVAE2 on 300Ver but with anomalies in the other three shapes. Specifically, among the images of the largest 30 (10% of the dataset) MSE values of each curve, the number of anomalies is listed in Table 2. From the table, the weighted MSE using any foreground map has a way high detection rate than the conventional MSE.

When taking multiple foreground maps from different methods into consideration, the top two results in Table 2 — YOLOv5 and KNN, inspire us to combine their foreground maps by applying Equation 3-6 in which w_1 (namely w_{YOLOv5}) and w_2 (namely w_{KNN}) are 0.52 and 0.48, respectively as the normalized values of 78.21% and 71.79%. To be noted is that any combination is possible no matter whether a supervised human detector is available.

To avoid being one-sided, we do further experiments with MNAD and CAE on 300Ver in a way of using rectangle-shaped anomalies and the foreground map combining YOLOv5 and KNN. By using the weighted MSE instead of the conventional MSE, the detection rate increases from 9.52% to 66.67% for MNAD and from 4.76% to 66.67% for CAE.

(a) Rectangle (b) Square (c) Circle (d) Ellipse

Figure 5: Examples of anomalies with “black-white-pixel” patterns in four different shapes.

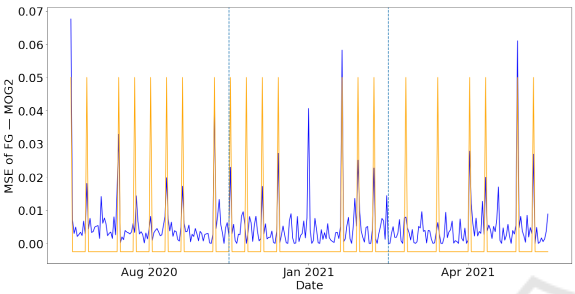

(a) MSE_{fg} of MOG2

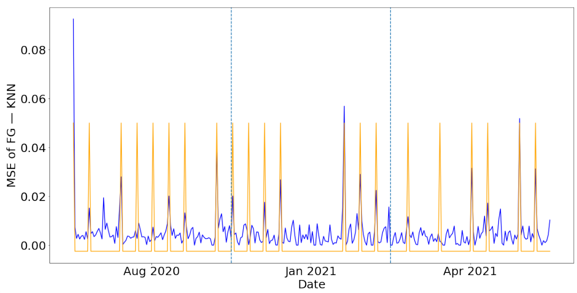

(b) MSE_{fg} of KNN

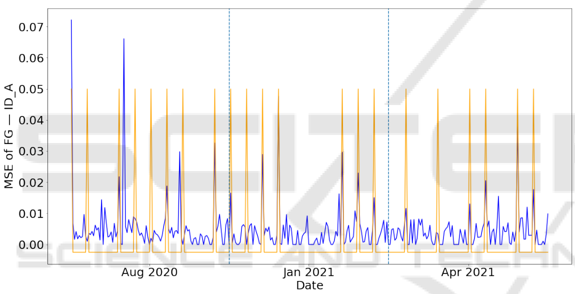

(c) MSE_{fg} of ID$_a$

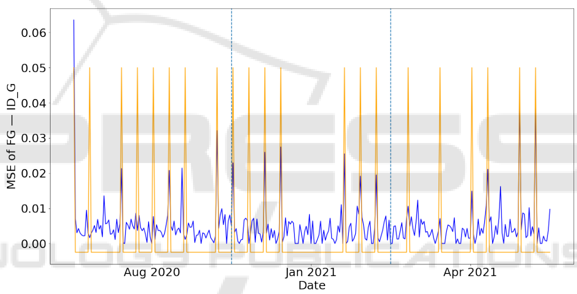

(d) MSE_{fg} of ID$_g$

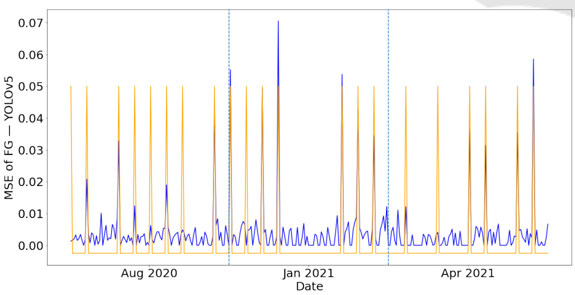

(e) MSE_{fg} of YOLOv5

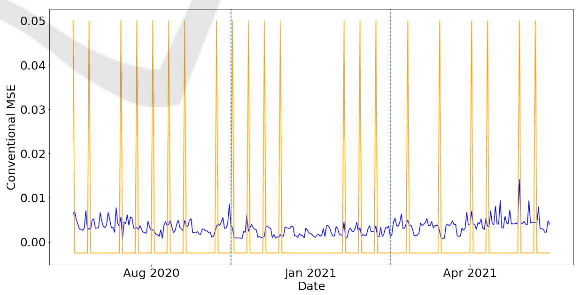

(f) MSE_{cvt}

Figure 6: After introducing rectangle-shaped anomalies, MSE curves across time from VQVAE2 on the 300Ver dataset. The blue curves describe the MSE changes, and the orange peaks indicate the locations of anomalies. The vertical azure dashed lines are used to separate different months.

As a whole, the proposed weighted MSE improves anomaly detection rate markedly on 300Ver — VQVAE2 (2.68 times-3.21 times), MNAD (7 times), CAE (14 times), verifying that this strategy is worth being incorporated in datasets or applications spanning a long time period.

4.3.3 Extended Experiments

The extended experiments on 3515Ver use rectangle-shaped “black-white-pixel” patterns overlapping on the persons who are near the horizontal edge of the water to simulate the anomalies. The resultant 60

Table 2: Anomaly detection results of weighted MSE and conventional MSE.

	Statistical Background				Object-centric Foreground	Conventional
	MOG2	KNN	ID_a	ID_g	YOLOv5	
Rectangle (21)	16	**17**	15	15	16	4
Square (21)	13	**14**	12	13	15	7
Circle (20)	11	**13**	10	10	16	4
Ellipse (16)	**14**	12	**14**	13	14	4
Sum (78)	54	**56**	51	51	61	19
Detection Rate	69.23%	**71.79%**	65.38%	65.38%	78.21%	24.36%

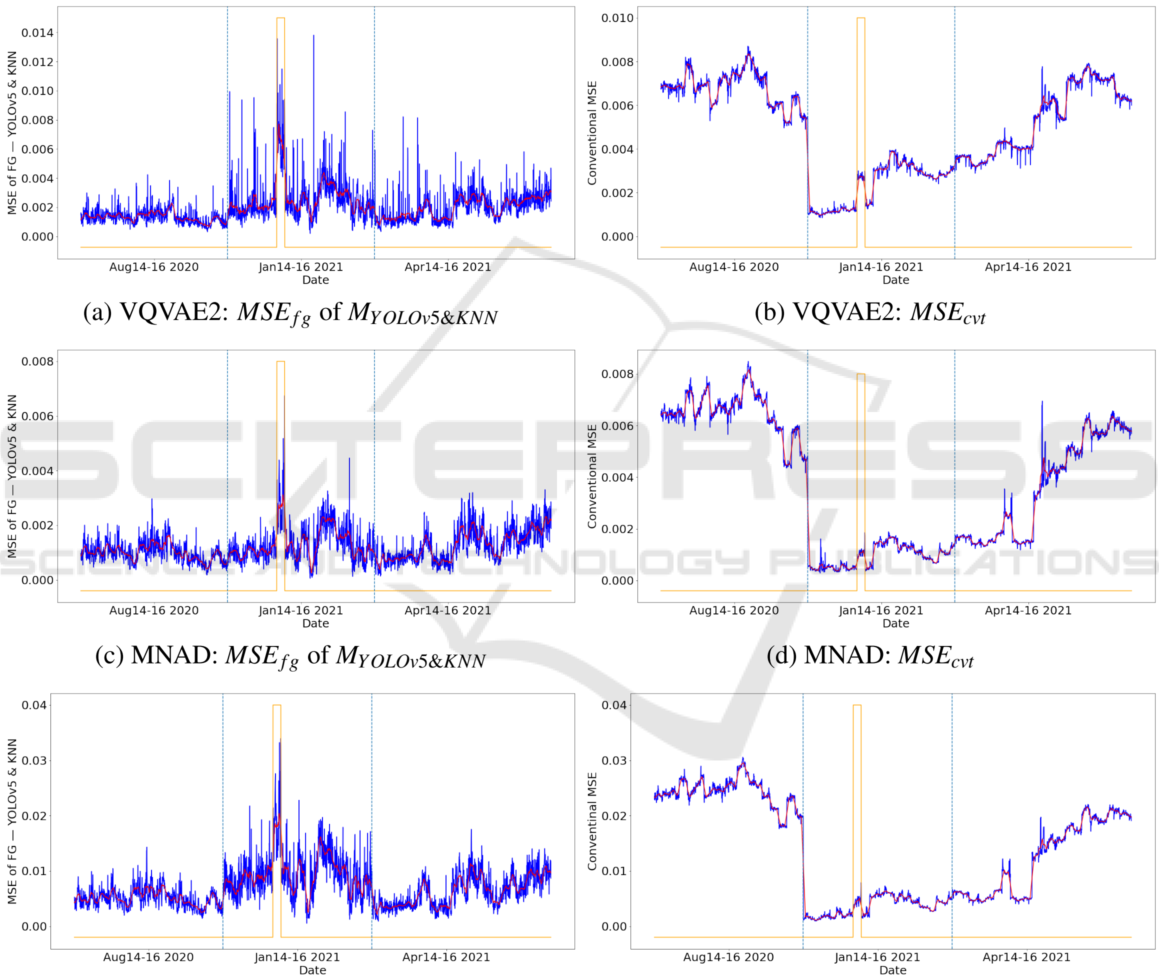

(a) VQVAE2: MSE_{fg} of $M_{YOLOv5\&KNN}$

(b) VQVAE2: MSE_{cvt}

(c) MNAD: MSE_{fg} of $M_{YOLOv5\&KNN}$

(d) MNAD: MSE_{cvt}

(e) CAE: MSE_{fg} of $M_{YOLOv5\&KNN}$

(f) CAE: MSE_{cvt}

Figure 7: MSE curves of VQVAE2, MNAD, and CAE on 3515Ver with synthesized rectangle-shaped anomalies. The curve of absolute MSE values is in blue. The curve of the smoothed values are in red. The anomalies are located with orange peaks. The vertical azure dashed lines are used to separate different months.

synthesized anomalies are consecutive frames and the persons overlapped with the abnormal pattern are fixed individuals. This increases the authenticity of the simulated anomalies — in real life an anomaly usually persists through multiple frames and involves fixed persons.

Figure 7 gives the MSE curves of the three AEs on 3515Ver with synthesized anomalies, in which the curves of absolute MSE values are in blue and the smoothed ones are in red, and the anomalies are located with orange peaks. In Figure 7, by using the weighted MSE with the foreground map $M_{YOLOv5\&KNN}$ combining YOLOv5 and KNN, the ascending peaks in (a), (c), and (e) accurately detect the anomalies, yet the conventional MSE curves in (b), (d), and (f) are entirely dominated by time-induced influences for example the fall of a cliff due to the seasonal transition between August 2020 and January 2021. We therefore believe that the extended experiments on a much larger dataset also prove the effectiveness of the proposed weighted MSE in anomaly detection.

5 CONCLUSIONS

This paper proposes a weighted reconstruction error in autoencoder-based anomaly detection for long-term surveillance systems. The method aims to make the calculated error more focused on the region where anomalies are assumed in and thus reduces the influence of time-induced environmental drift.

We apply three selected autoencoders to three-month datasets to test the anomaly detection performance. With synthesized anomalies, the autoencoder with proposed weighted reconstruction error always gets a much higher detection rate (more than twice) than the conventional reconstruction error version where each pixel contributes the same, which proves the usefulness of the proposed strategy.

This method is implemented as a flexible module, therefore we expect it can be integrated into and verified by more frameworks. Besides, as a study at harbor fronts, in the future we will use this method to detect emergencies and potentially dangerous incidents like traffic accidents, drowning accidents, crowds in coronavirus days, etc., so that timely controls or rescues by polices, safeguards, and other professionals can be provided for a safer life.

ACKNOWLEDGEMENTS

This work is funded by TrygFonden as part of the project Safe Harbor.

REFERENCES

Adam, A., Rivlin, E., Shimshoni, I., and Reinitz, D. (2008). Robust real-time unusual event detection using multiple fixed-location monitors. *IEEE transactions on pattern analysis and machine intelligence*, 30(3):555–560.

Akilan, T., Wu, Q. J., Safaei, A., Huo, J., and Yang, Y. (2019). A 3d cnn-lstm-based image-to-image foreground segmentation. *IEEE Transactions on Intelligent Transportation Systems*, 21(3):959–971.

Babaee, M., Dinh, D. T., and Rigoll, G. (2018). A deep convolutional neural network for video sequence background subtraction. *Pattern Recognition*, 76:635–649.

Bradski, G. (2000). The OpenCV Library. *Dr. Dobb's Journal of Software Tools*.

Chong, Y. S. and Tay, Y. H. (2017). Abnormal event detection in videos using spatiotemporal autoencoder. In *International Symposium on Neural Networks*, pages 189–196. Springer.

Deepak, K., Chandrakala, S., and Mohan, C. K. (2020). Residual spatiotemporal autoencoder for unsupervised video anomaly detection. *Signal, Image and Video Processing*, pages 1–8.

Fu, J., Fan, W., and Bouguila, N. (2018). A novel approach for anomaly event detection in videos based on autoencoders and se networks. In *2018 9th International Symposium on Signal, Image, Video and Communications (ISIVC)*, pages 179–184. IEEE.

Georgescu, M.-I., Tudor Ionescu, R., Shahbaz Khan, F., Popescu, M., and Shah, M. (2020). A scene-agnostic framework with adversarial training for abnormal event detection in video. *arXiv e-prints*, pages arXiv–2008.

Gong, D., Liu, L., Le, V., Saha, B., Mansour, M. R., Venkatesh, S., and Hengel, A. v. d. (2019). Memorizing normality to detect anomaly: Memory-augmented deep autoencoder for unsupervised anomaly detection. In *Proceedings of the IEEE/CVF International Conference on Computer Vision*, pages 1705–1714.

Hasan, M., Choi, J., Neumann, J., Roy-Chowdhury, A. K., and Davis, L. S. (2016). Learning temporal regularity in video sequences. In *Proceedings of the IEEE conference on computer vision and pattern recognition*, pages 733–742.

Ionescu, R. T., Khan, F. S., Georgescu, M.-I., and Shao, L. (2019). Object-centric auto-encoders and dummy anomalies for abnormal event detection in video. In *Proceedings of the IEEE/CVF Conference on Computer Vision and Pattern Recognition*, pages 7842–7851.

Liu, J., Philipsen, M. P., and Moeslund, T. B. (2021a). Supervised versus self-supervised assistant for surveillance of harbor fronts. In *VISIGRAPP (5: VISAPP)*, pages 610–617.

Liu, J., Song, K., Feng, M., Yan, Y., Tu, Z., and Zhu, L. (2021b). Semi-supervised anomaly detection with dual prototypes autoencoder for industrial surface inspection. *Optics and Lasers in Engineering*, 136:106324.

Lu, C., Shi, J., and Jia, J. (2013). Abnormal event detection at 150 fps in matlab. In *Proceedings of the IEEE international conference on computer vision*, pages 2720–2727.

Luo, W., Liu, W., and Gao, S. (2017). In *Proceedings of the IEEE International Conference on Computer Vision*, pages 341–349.

Mahadevan, V., Li, W., Bhalodia, V., and Vasconcelos, N. (2010). Anomaly detection in crowded scenes. In *2010 IEEE Computer Society Conference on Computer Vision and Pattern Recognition*, pages 1975–1981. IEEE.

Mehran, R., Oyama, A., and Shah, M. (2009). Abnormal crowd behavior detection using social force model. In *2009 IEEE Conference on Computer Vision and Pattern Recognition*, pages 935–942. IEEE.

Nguyen, T.-N. and Meunier, J. (2019). Anomaly detection in video sequence with appearance-motion correspondence. In *Proceedings of the IEEE International Conference on Computer Vision*, pages 1273–1283.

Nikolov, I. A., Philipsen, M. P., Liu, J., Dueholm, J. V., Johansen, A. S., Nasrollahi, K., and Moeslund, T. B. (2021). Seasons in drift: A long-term thermal imaging dataset for studying concept drift. In *Thirty-fifth Conference on Neural Information Processing Systems*.

Park, H., Noh, J., and Ham, B. (2020). Learning memory-guided normality for anomaly detection. In *Proceedings of the IEEE/CVF Conference on Computer Vision and Pattern Recognition*, pages 14372–14381.

Pranav, M., Zhenggang, L., et al. (2020). A day on campus-an anomaly detection dataset for events in a single camera. In *Proceedings of the Asian Conference on Computer Vision*.

Razavi, A., van den Oord, A., and Vinyals, O. (2019). Generating diverse high-fidelity images with vq-vae-2. In *Advances in neural information processing systems*, pages 14866–14876.

Song, H., Sun, C., Wu, X., Chen, M., and Jia, Y. (2019). Learning normal patterns via adversarial attention-based autoencoder for abnormal event detection in videos. *IEEE Transactions on Multimedia*.

Tsai, D.-M. and Jen, P.-H. (2021). Autoencoder-based anomaly detection for surface defect inspection. *Advanced Engineering Informatics*, 48:101272.

Ultralytics (2020). Yolov5. last accessed: October 25, 2021.

Yue, H., Wang, S., Wei, J., and Zhao, Y. (2019). Abnormal events detection method for surveillance video using an improved autoencoder with multi-modal input. In *Optoelectronic Imaging and Multimedia Technology VI*, volume 11187, page 111870U. International Society for Optics and Photonics.

Zivkovic, Z. (2004). Improved adaptive gaussian mixture model for background subtraction. In *Proceedings of the 17th International Conference on Pattern Recognition, 2004. ICPR 2004.*, volume 2, pages 28–31. IEEE.

Zivkovic, Z. and Van Der Heijden, F. (2006). Efficient adaptive density estimation per image pixel for the task of background subtraction. *Pattern recognition letters*, 27(7):773–780.